Journal of Materials Chemistry B

ROYAL SOCIETY OF CHEMISTRY

PAPER

View Article Online
View Journal | View Issue

Cite this: J. Mater. Chem. B, 2025, 13, 12536

Oligothiophene-based photosensitizers with tunable push–pull architectures: design, synthesis and characterization

Soraia Flammini,†[a] Manuele Di Sante,†[bc] Paolo Emidio Costantini,†[cd] Edoardo Jun Mattioli,[bc] Alessia Marconi,[bc] Eleonora Turrini,[e] Silvia la Rosa,[e] Maria Montrone,[b] Tainah Dorina Marforio,[bc] Michela Nigro,[cd] Nicol Spallacci,[a] Alberto Zanelli,[a] Mattia Zangoli,[a] Alberto Danielli,[cd] Matteo Di Giosia,*[bc] Francesca Di Maria*[a] and Matteo Calvaresi*[bc]

Donor–acceptor–donor (D–A–D) thiophene-based compounds, characterized by thiophene as a donor unit and benzothiadiazole (Bz) as an acceptor, represent an emerging class of theranostic agents for imaging and photodynamic therapy. Here, we expand this class of molecules by strategically varying the position of the electron-accepting unit within the oligothiophene (OT) backbone structure, realizing a series of different push–pull architectures (A–D, D–A–D, and D–A). This rational design allows for precise modulation of key photophysical parameters, including absorption and emission spectra, molar absorption coefficient, charge separation, and frontier molecular orbitals. Computational predictions indicate that all the designed oligothiophene molecules possess the photophysical properties to be effective photosensitizers (PSs), prompting their chemical synthesis. To enable the use of insoluble oligothiophenes in physiological environments as PSs, an *N*-succinimidyl (NHS) ester group is introduced in the molecules (NHS–OT), to allow the subsequent conjugation with human serum albumin (HSA). The effective conjugation of the oligothiophenes to the protein (HSA–OT) is confirmed by mass spectrometry and electrophoresis. The HSA–OT bioconjugates are soluble in a physiological environment, exhibit intrinsic bright fluorescence and are non-toxic under dark conditions. Upon irradiation, the bioconjugates efficiently generate reactive oxygen species, following both type I and type II mechanisms, and lead to the complete eradication of cancer cells at much lower concentrations (IC_{50} = 4.0 nM for the most efficient PS) than common photosensitizers. Real-time fluorescence imaging revealed rapid membrane blebbing when the cells treated with HSA–OT were exposed to light, indicative of necrotic-like immunogenic cell death. Taken together, our findings highlight the power of molecular engineering in optimizing photosensitizer performance and provide proof of concept for the potential of HSA–OT conjugates as a multifunctional theranostic platform for cancer.

Received 6th May 2025,
Accepted 8th August 2025

DOI: 10.1039/d5tb01076d

rsc.li/materials-b

Introduction

Push–pull photosensitizers (PSs) are a class of molecules designed with electron-donating (push) and electron-withdrawing (pull) groups to enhance their photophysical and photochemical properties for photodynamic therapy (PDT).[1–4] This molecular architecture improves light absorption, charge separation, and reactive oxygen species (ROS) generation, making them highly effective for cancer treatment.[1,2] This design facilitates intramolecular charge transfer (ICT), resulting in: (i) the promotion of intersystem crossing,[5,6] crucial for PDT efficacy and (ii) improved photostability of the molecules.[7]

Thanks to the modular nature of donor and acceptor units, a variety of structural configurations, such as D–A, D–A–D, or

[a] Istituto per la Sintesi Organica e la Fotoreattività (ISOF) – Consiglio Nazionale delle Ricerche, Via Piero Gobetti, 101, Bologna 40129, Italy. E-mail: francescagiulia.dimaria@cnr.it
[b] Dipartimento di Chimica "Giacomo Ciamician", Alma Mater Studiorum – Università di Bologna, Via Piero Gobetti, 85, Bologna 40129, Italy. E-mail: matteo.digiosia2@unibo.it, matteo.calvaresi3@unibo.it
[c] IRCCS Azienda Ospedaliero – Universitaria di Bologna, Preclinical & Translational Research in Oncology lab (PRO), Bologna 40138, Italy
[d] Dipartimento di Farmacia e Biotecnologie, Alma Mater Studiorum – Università di Bologna, Via Francesco Selmi 3, Bologna 40126, Italy
[e] Dipartimento di Scienze per la Qualità della Vita; Alma Mater Studiorum – Università di Bologna, Corso D'Augusto, 237, Rimini 47921, Italy
† These authors contributed equally to this work.

A–D–A, can be designed.[1–4,8] This structural flexibility allows precise tuning of their photophysical properties and phototherapeutic performance.[1,2] Moreover, functional groups can be readily incorporated into the molecular backbone to enhance their water solubility or impart specific targeting capabilities to the photosensitizers.[9] Originally developed as organic semiconductor materials for applications in organic light-emitting diodes (OLEDs), organic solar cells (OSCs), and organic field-effect transistors (OFETs), these molecules have, over the past few decades, found rapidly expanding roles in the biomedical field, including biosensing, bioimaging, and cancer phototherapy.

Thiophenes, a class of five-membered sulfur-containing heterocycles, have gained increasing attention in the field of PDT due to their unique electronic properties and structural versatility.[10–14] Their photostability and strong electron-donating ability make them ideal building blocks for constructing donor–acceptor or push–pull type photosensitizers.

We recently showed that an oligothiophene compound (OT) with the D–A–D structure, *i.e.* 4-([2,2′-bithiophen]-5-yl)-7-(thiophen-2-yl)benzo[*c*][1,2,5]thiadiazole, characterized by thiophene as the donor unit and benzothiadiazole (Bz) as the acceptor (Fig. 1, compound **2**),[15,16] is highly photoactive and its *N*-hydroxysuccinimide derivative can be conjugated with human serum albumin (HSA–OT) to improve its solubility in physiological environments.[11,12] The HSA–OT bioconjugate is a novel theranostic platform able to generate ROS intracellularly, leading to the complete eradication of cancer cells upon irradiation, and, at the same time, provide imaging contrast through the intrinsic fluorescence of the oligothiophene.[11] However, the tetrameric structure of this molecule offers further opportunities for molecular engineering: the Bz unit can, in principle, be placed at any of the four thiophene positions, giving rise to different electronic distributions and push–pull strengths. In this study, we set out to investigate how changing the position of the Bz unit within the same tetrameric scaffold affects the optical, electronic, and biological behavior of the resulting compounds. By shifting the Bz to positions 1, 3, and 4 – while keeping the overall conjugated system constant – we generated a library of regioisomers with distinct A–D, D–A–D, and D–A characteristics (Fig. 1). This structural variation allowed us to probe the subtle interplay between molecular architecture and function for this class of oligothiophenes.

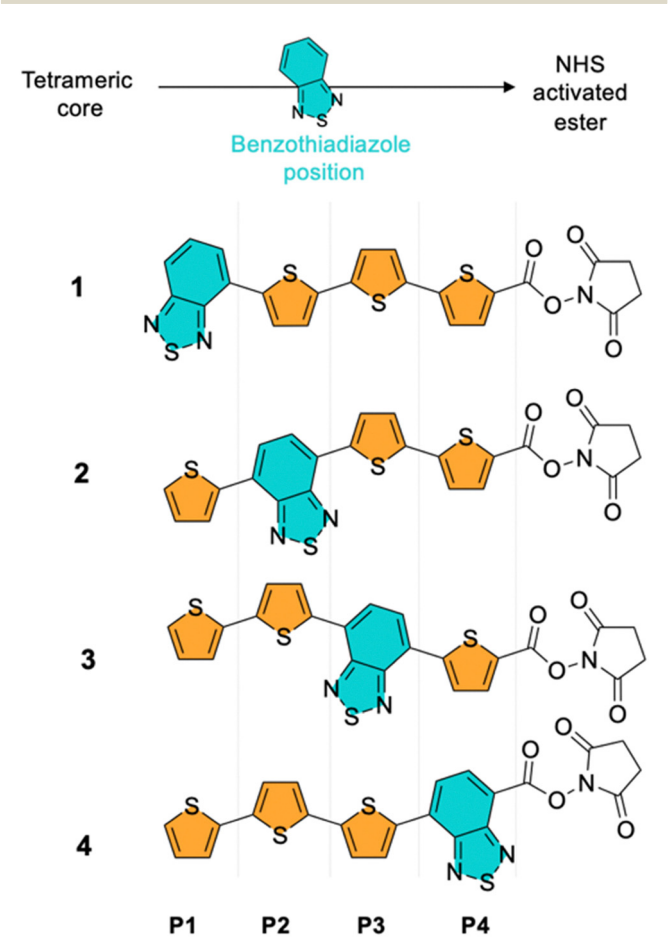

Fig. 1 Molecular structures of different push–pull oligothiophenes functionalized with a terminal *N*-succinimidyl ester (NHS) group.

Results and discussion

Computational design of the OT compounds

Photosensitizers can produce reactive oxygen species (ROS) through two different mechanisms:[17] (i) type I process, which is based on an electron transfer process and produces the superoxide radical anion (eqn (1)) and other reactive oxygen species such as hydrogen peroxide or hydroxyl radicals and (ii) type II mechanism, which is based on an energy transfer process and generates singlet oxygen (eqn (2)).

$$PS^{\bullet(-)} + O_2 \rightarrow PS + O_2^{\bullet(-)} \quad (1)$$

$$PS(T_1) + {}^3O_2 \rightarrow PS\ (S_0) + {}^1O_2 \quad (2)$$

The formation of $O_2^{\bullet(-)}$ can happen through the transfer of an electron from the reduced PS (PS^-) to molecular oxygen (O_2), producing the superoxide anion.[18] Reaction energy calculations (Table 1) show that all compounds **1–4** can follow the type I mechanism.

Once the superoxide anion is generated, it can serve as a precursor to several other ROS, such as hydrogen peroxide, hydroxyl radicals and other radical oxygen species.[17,18]

TD-DFT calculations of singlet and triplet low-lying levels of molecules **1–4** suggest that all the compounds can also produce ROS following the type II mechanism: (i) we compared the S_0–T_1 energy gap of compounds **1–4** with the energy needed to

Table 1 Thermodynamics of the electron transfer reaction between the reduced form of the photosensitizer and molecular oxygen (eqn (1))

OT	ΔE $PS^{\bullet(-)} + O_2 \rightarrow PS + O_2^{\bullet(-)}$ (kcal mol^{-1})
1	−11.5
2	−8.0
3	−4.1
4	−0.1

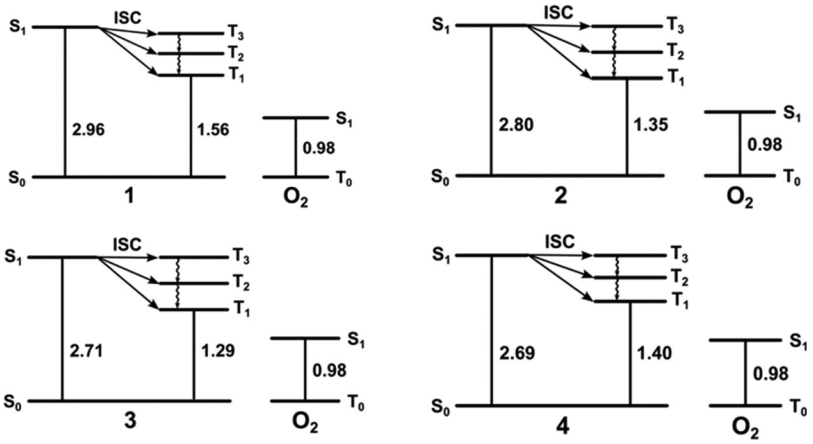

Fig. 2 TD-DFT calculations of singlet and triplet low-lying levels of compounds **1–4** together with the comparison with the oxygen levels.

excite oxygen from $^3O_2$ to $^1O_2$ (0.98 eV). The lowest triplet state energies (T_1) of compounds **1–4** are always located above the singlet oxygen state (Fig. 2); (ii) the amplitude of the spin–orbit coupling (SOC) constants (Table 2), which determines the efficiency of the intersystem crossing (ISC) process, is much higher than the threshold value commonly set at 0.24 cm^{-1}.[19,20] To determine whether the designed PS may have an effective coupling channel from S_1 to T_n, the SOC of S_1–T_n (T_1–T_3) was computed (Table 2, see SI for computational details).

Since these results indicate that the new push–pull oligomers **1**, **3**, and **4** are promising photosensitizers that can produce ROS through both type I and type II processes, we proceeded with their synthesis.

Synthesis and characterization of the OT compounds

From a synthetic point of view, accessing specific positional isomers often requires distinct synthetic routes or strategies. The target thiophene-based oligomers (OT) were synthesized following the synthetic strategy outlined in Scheme 1. All molecules (*i.e.*, thiophene-based tetramers) were designed to carry a terminal *N*-succinimidyl ester (NHS–OT) moiety to enable their covalent conjugation with human serum albumin (HSA). The positional shift of the Bz unit within the tetramer core was accomplished through cross-coupling reactions between appropriately functionalized halogenated and metallated intermediates.[21,22] For compound **4**, the *N*-succinimidyl (NHS) ester group was introduced through a functional group interconversion strategy, which involves the oxidation of an aldehyde to a carboxylic acid, followed by esterification with *N*-hydroxysuccinimide. Compounds **1** and **4** were synthesized *via* Stille coupling, in which a brominated precursor bearing the NHS moiety (**1d**, **4c**) was coupled with either a stannylated thiophene dimer (**1c**) or trimer (**4d**). Compounds **2** and **3** were synthesized using microwave-assisted Suzuki cross-coupling of a boronated (**2d**) or brominated (**3d**) thiophene unit containing the NHS ester with a complementary brominated or boronated trimer (**2c** or **3c**), see SI for details.

Table 2 Computed SOC magnitudes and energy gaps between S_1 and T_1–T_3 states for compounds **1–4**

OT	SOC_{11} (cm^{-1})	ΔE_{11} (eV)	SOC_{12} (cm^{-1})	ΔE_{12} (eV)	SOC_{13} (cm^{-1})	ΔE_{13} (eV)
1	2.37	1.31	4.70	0.93	11.38	0.28
2	0.47	1.33	2.34	0.64	2.65	−0.20
3	9.83	1.28	23.96	0.37	7.31	−0.03
4	2.03	1.15	3.51	0.51	6.65	−0.17

All molecules were obtained in good yields (45–60%) and fully characterized using spectroscopic techniques (see Fig. S1–S11). Notably, compounds **1** and **4** exhibited enhanced solubility and processability in common organic solvents compared to the benchmark molecule **2**, facilitating purification procedures and making them more suitable for further functionalization and integration into biological applications.

We observed how this systematic structural modification governs the electronic/photophysical properties of the conjugated system. Shifting the electron-accepting Bz unit along the conjugated backbone, for a fixed oligomer length, modifies the sequence and strength of donor–acceptor interactions, leading to variations in the overall electronic structure of the molecule. As the benzothiadiazole moves from position **1** to position **4** (approaching the activated ester group), a progressive red shift is observed in both the absorption (**1** (445 nm) < **2** (476 nm) < **3** (489 nm) < **4** (492 nm)) and emission (**1** (606 nm) < **2** (611 nm) < **3** (648 nm) < **4** (680 nm)) spectra (Fig. 3A and Table S1). The UV-vis spectra calculated at the TD-DFT level (see computational details) well reproduce the experimental ones (Fig. S12), validating the accuracy of the calculations. The computed HOMO–LUMO gap is reduced passing from compound **1** to compound **4** (Fig. 3B), clearly explaining the observed red shift. The position of the acceptor group (Bz unit) strongly influences its acceptor strength, as observed by the sum of the charges on the Bz ring in the different positions (Fig. S13). In fact, passing from position 1 (−0.04*e*) to position 4 (−0.17*e*) the acceptor group strength increases, and a larger

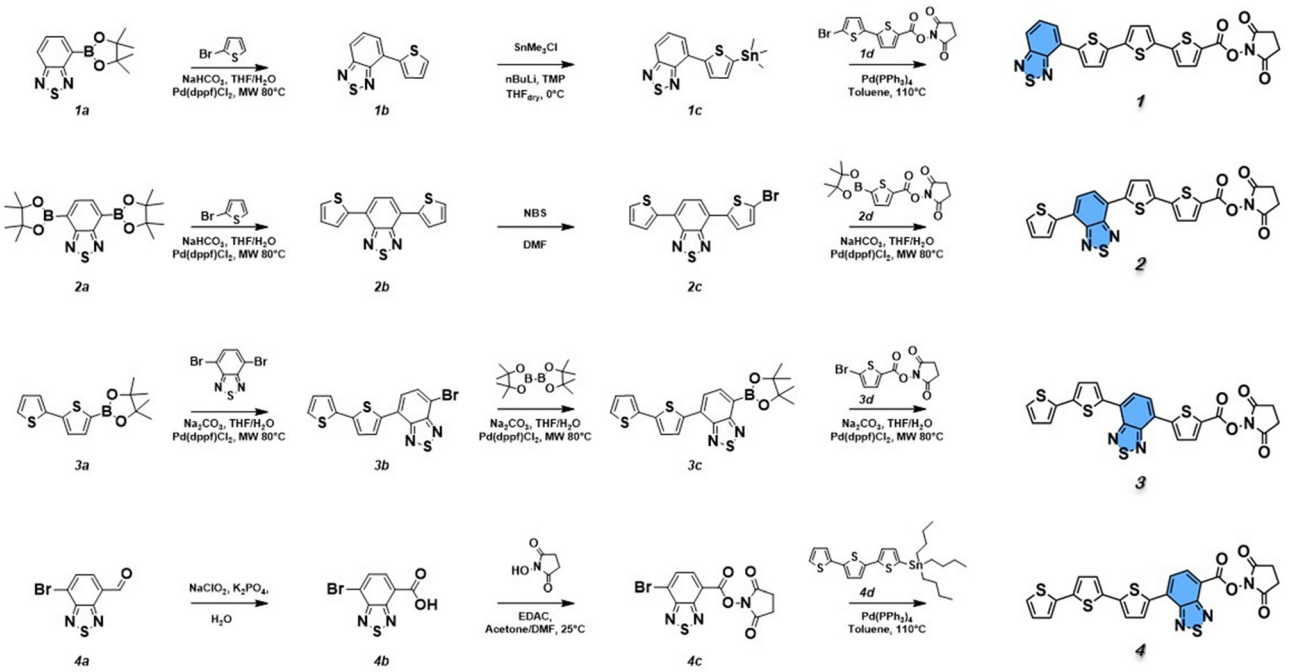

Scheme 1 Synthesis scheme of compounds **1–4**. **2** was synthesized according to ref. 23.

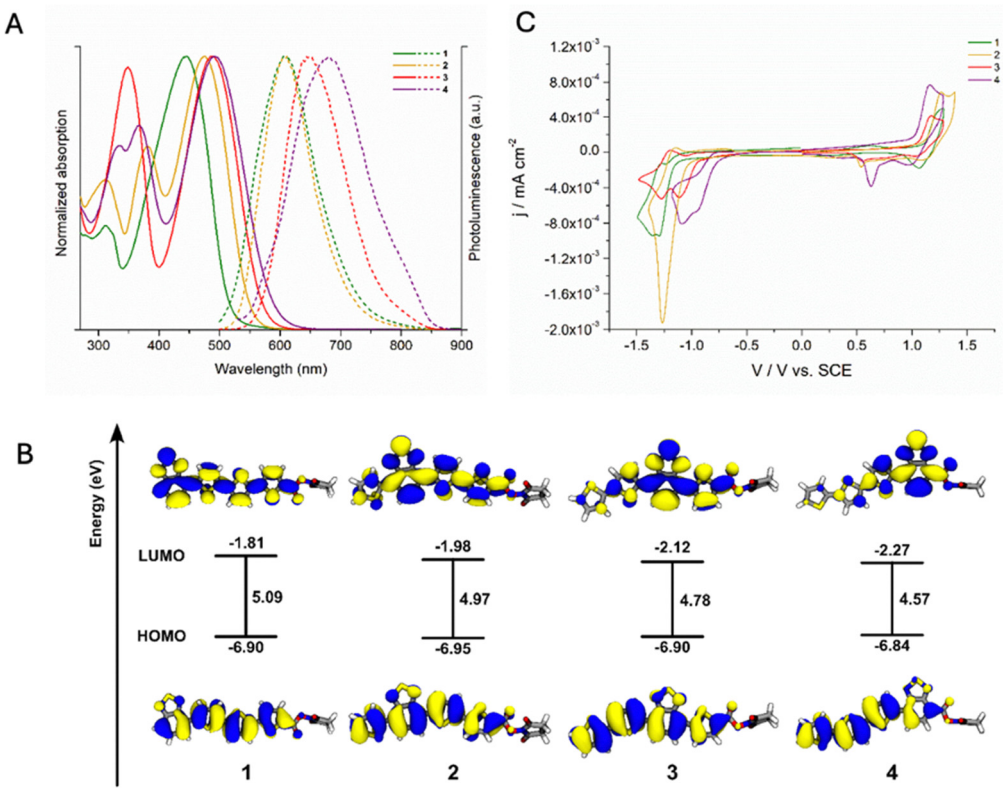

Fig. 3 (A) UV-vis absorption (solid line) and emission (dashed line) spectra of compounds **1** (green line), **2** (orange line), **3** (red line) and **4** (purple line) in DMF. (B) Calculated HOMO–LUMO energies of compounds **1–4** and the corresponding energy gaps. (C) Cyclic voltammetry of compounds **1–4** in CH_2Cl_2.

value of negative charge is accumulated on the Bz ring and the UV-vis absorption spectrum moves toward longer wavelengths.

For all compounds the absorption band that is characterized by the strongest intensity corresponds to the $S_0 \rightarrow S_1$ transition. The HOMO–LUMO orbitals (Fig. 3B), and the natural transition orbitals (NTO, Fig. S14), clearly show that the $S_0 \rightarrow S_1$ transitions of compounds **1–4** correspond to $\pi \rightarrow \pi^*$ excitation, from the delocalized π system of the four rings to the localized π^* orbital of the acceptor Bz unit.

Analysis of the charges in the S_1 excited state revealed quantitatively a strong localization of negative charges on the Bz ring, evidencing the charge transfer (CT) character of the $S_0 \rightarrow S_1$ transition, especially passing from compound **1** to **4** (Δq: $-0.06 < -0.14 < -0.19 < -0.32$, Fig. S13).

The optimized geometries of the S_1 state for compounds **1–4** (Fig. S15 and Table S2) are characterized by strong planarization of the molecule, significantly resembling the T_1 state geometry, possibly explaining the high values obtained for the SOC.

Fig. 3C shows the cyclic voltammetry of the four tetramers recorded in CH_2Cl_2. The positional shift of the Bz unit has a significant effect on the reduction potentials, which become progressively less negative as the acceptor unit moves closer to the NHS ester (Table S3) ($E^\circ_{red} \rightarrow 1(-1.31\,V) < 2(-1.20\,V) < 3(-1.02\,V) < 4(-0.83\,V)$), indicating a remarkable increase in the electron affinity of the materials, as observed also by the DFT calculations that show a significant lowering of the LUMO energy passing from compound **1** to **4**.

In particular, compounds **1**, **3**, and **4** exhibit bielectronic reduction waves, suggesting that each molecule can accommodate two electrons at rather close potentials ranging from 0.06 V to 0.17 V.[24] In contrast, the reduction of compound **2** appears as a single wave. However, considering the behavior of the other parent derivatives, it is reasonable to infer that the reduction of compound **2** is also a bielectronic process, albeit occurring at a single potential rather than at two distinct potentials.

Conversely, the positional shift of the Bz unit has a minor impact on the oxidation potentials (Table S3), which slightly decrease from compounds **1** and **2** to compounds **3** and **4** ($E^\circ_{ox} \rightarrow 1(1.16\,V) \approx 2(1.18\,V) > 3(1.09\,V) \approx 4(1.07\,V)$). Also in this case, the data are in agreement with DFT calculations that show a minimal perturbation of the energy levels of the HOMO in compounds **1–4**. Furthermore, except for compound **1**, all molecules exhibit a quasi-reversible oxidation wave with two reverse peaks. The appearance of the second reverse peak at lower potentials could be ascribed to the decomposition of the oxidized species (*i.e.*, radical cation), potentially arising from dimerization or degradation processes. These results indicate that compound **1** exhibits better stability and reversibility in the oxidation and reduction processes compared to the other compounds in this series.

Synthesis and characterization of HSA–OT bioconjugates

Exploiting the *N*-succinimidyl ester (NHS) moiety of the oligothiophene derivatives (NHS–OT), compounds **1**, **2**, **3**, and **4** were conjugated to HSA, targeting primary amines of the protein (Fig. 4A).[11,12,24,25] The bioconjugation of the oligothiophenes with the protein (HSA–OT) promotes their solubility in physiological environments, overcoming the limitation of

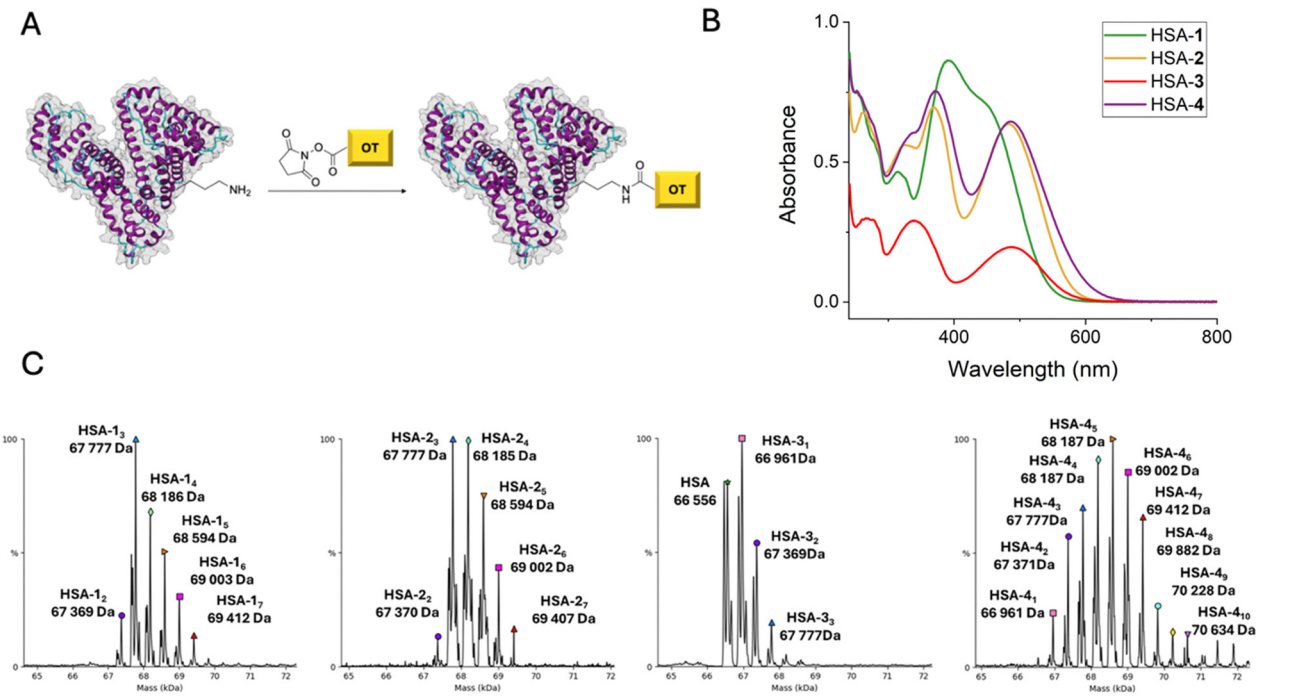

Fig. 4 (A) Conjugation of oligothiophene *N*-hydroxysuccinimidyl esters, NHS–OT, to HSA. (B) Absorption spectra of HSA-**1** (green line), HSA-**2** (orange line), HSA-**3** (red line) and HSA-**4** (purple line) in PBS. (C) Deconvolved mass distributions of the HSA-**1**, HSA-**2**, HSA-**3** and HSA-**4** bioconjugates. The subscripts indicate the number of molecules bound to HSA.

aqueous insolubility that hampers their exploitation in nanomedicine.

The formation of the amidic bond in place of the NHS group modifies the UV-vis (Fig. 4B and Fig. S16) and emission (Fig. S17) spectra of OT compounds, suggesting the covalent attachment of OT to HSA. In particular, the absorption peak at ~380 nm (Fig. 4B and Fig. S16) was blue shifted and increased in intensity for the bioconjugate, due to the formation of the amidic bond between the OT derivative and the amine groups of the proteins.[12]

Considering the starting HSA concentration and the molar absorption coefficients of the four oligothiophenes, an average of 4.2 (**1**), 3.9 (**2**), 1.4 (**3**) and 4.4 (**4**) OT molecules were conjugated per HSA protein. Deconvolved mass distribution obtained from the mass spectra of the HSA–OT bioconjugates (Fig. 4C) agrees with the results obtained from UV-vis characterization and shows in more detail the distribution of the OT/HSA population. Electrophoretic characterization, performed both under native and denaturing conditions, unambiguously supports the conjugation of the oligothiophenes to the protein (Fig. S18 and S19). In fact, the fluorescent spots originating from OT perfectly match the protein bands, revealed after Coomassie staining. Dynamic light scattering (DLS) data (Table 3) showed that HSA-**1**, HSA-**2**, and HSA-**4** bioconjugates maintain their monomeric structure under physiologically relevant conditions, while HSA-**3** shows a tendency to form aggregates around 60 nm in size. The propensity of HSA-**3** to aggregate can influence both reactive oxygen species (ROS) production and cellular uptake. Aggregation has been shown to critically modulate ROS generation by photosensitizers, with both aggregation-induced ROS generation and aggregation-caused quenching observed experimentally.[26] Moreover, while aggregation may reduce receptor-mediated uptake of HSA, it can concurrently enhance endocytosis-mediated internalization pathways.

The ability of the different HSA–OT bioconjugates to produce ROS, upon irradiation, was determined by spectrophotometric measurements, as shown in Fig. 5, and benchmarked against Rose Bengal, a widely used reference photosensitizer. The production of peroxides (type I mechanism) was quantified using the Amplex Red assay while the generation of singlet oxygen generated was determined by the ABMDMA assay (see details in SI).[27–32]

The results showed that HSA–OT bioconjugates are characterized by a high photoactivity and generate ROS following both type I and type II mechanisms, confirming the computational results.

Notably, the type I photochemical pathway is highly active compared to Rose Bengal. In this system, ROS generation is further enhanced by the electron-rich residues of HSA within the HSA–OT bioconjugate, which participate in the electron transfer events required to produce oxygen radicals. While the type I mechanism typically relies on external sacrificial electron donors, in the HSA–OT complex the process is intrinsically driven by the protein itself. This finding is particularly noteworthy, as the discovery of new type I PSs is a rapidly evolving field for several reasons: unlike type II PSs, they remain active in hypoxic tumor environments, rely less on molecular oxygen, and generate a broader spectrum of ROS, enabling more extensive and potent anticancer effects.

Table 3 Diameters of HSA–OT bioconjugates measured by dynamic light scattering analysis

	Size (nm)	SD[a]
HSA	6.83	1.21
HSA-**1**	6.95	1.34
HSA-**2**	6.71	1.62
HSA-**3**	60.1	17.8
HSA-**4**	10.7	2.20

[a] Standard deviations (SD) calculated from three technical replicates.

Cellular uptake of the HSA–OT bioconjugates in A431 cells

Human epidermoid carcinoma A431 cells were used to evaluate *in vitro* the cellular uptake of the HSA–OT bioconjugates. By taking advantage of the intrinsic fluorescence of the oligothiophene compounds, it is possible to observe the cellular localization of the HSA–OT bioconjugates and quantify their uptake (Fig. 6).

Fluorescence confocal microscopy images of the A431 cells incubated with the HSA–OT bioconjugates (Fig. 6A–D) clearly show the intrinsic fluorescence of the bioconjugates, localized in the cellular membrane and in the cytoplasmatic compartment. The aggregation tendency of HSA-**3** is also confirmed through microscopy studies (Fig. 6C). Cellular uptake and internalization were also quantitatively demonstrated through flow cytometry experiments. Specifically, analysis of mean fluorescence intensity in cancer cells after incubation with the bioconjugates demonstrated the highest uptake for HSA-**4** bioconjugates, followed by HSA-**2**, HSA-**1** and HSA-**3** (Fig. 6E and F).

Cytotoxicity and phototoxicity of HSA–OT bioconjugates in A431 cells

In vitro tests using A431 cells were also used to evaluate the cytotoxicity and phototoxicity of the HSA–OT bioconjugates (Fig. 7). When cells were cultured with the HSA–OT bioconjugates in the dark, no significant decrease in cell viability was observed for all bioconjugates tested, even at the highest concentration (1 μM). These data demonstrated that HSA–OT bioconjugates are biocompatible and exhibit no "dark toxicity" (Fig. 7A).

In contrast, when A431 cells were incubated with HSA–OT bioconjugates and exposed to light, a dose-dependent decrease in cell viability was observed even at modest light doses (24 mW cm^{-2}) and at very low HSA–OT bioconjugate concentrations, in the nanomolar (nM) range (Fig. 7B). Complete eradication of the cancer cells was observed for all the HSA–OT bioconjugates, upon irradiation. HSA-**1** (IC_{50} = 4.0 nM) and HSA-**4** (IC_{50} = 7.3 nM) were the most efficient photosensitizers and showed superior performance compared to the original HSA-**2** (IC_{50} = 38.6 nM)[11] compound and HSA-**3**

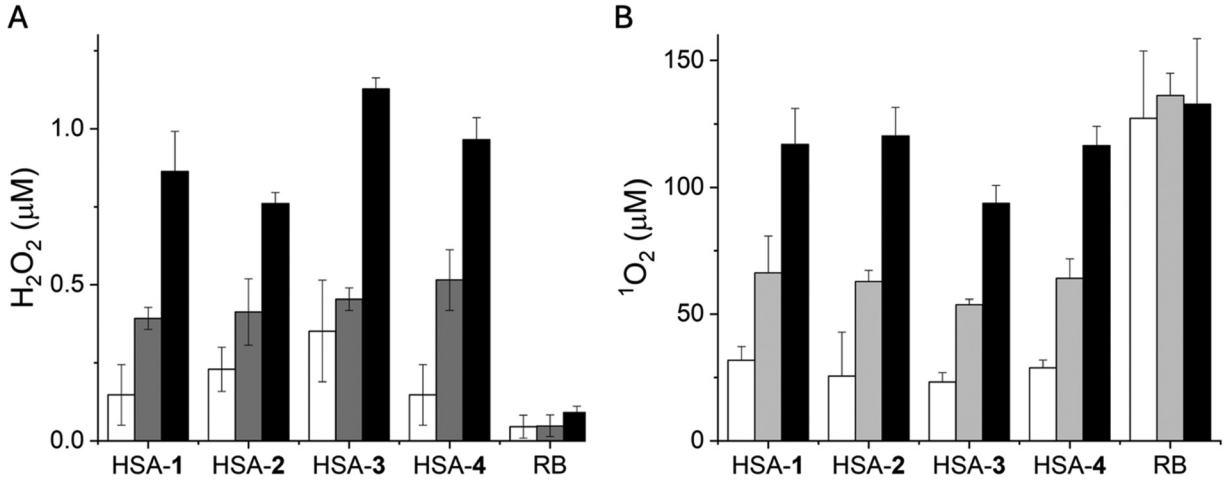

Fig. 5 Generation of ROS after 30 minutes of irradiation with a white LED (24 mW cm^{-2}). (A) Quantification of the production of hydrogen peroxide (type I mechanism) *via* the Amplex Red fluorometric assay. (B) Quantification of $^1O_2$ production (type II mechanism) using the ABMDMA colorimetric assay. Three different concentrations of the bioconjugates and rose Bengal (RB) as standard photosensitizers were tested: 100 nM (white bars), 300 nM (gray bars) and 1000 nM (black bars).

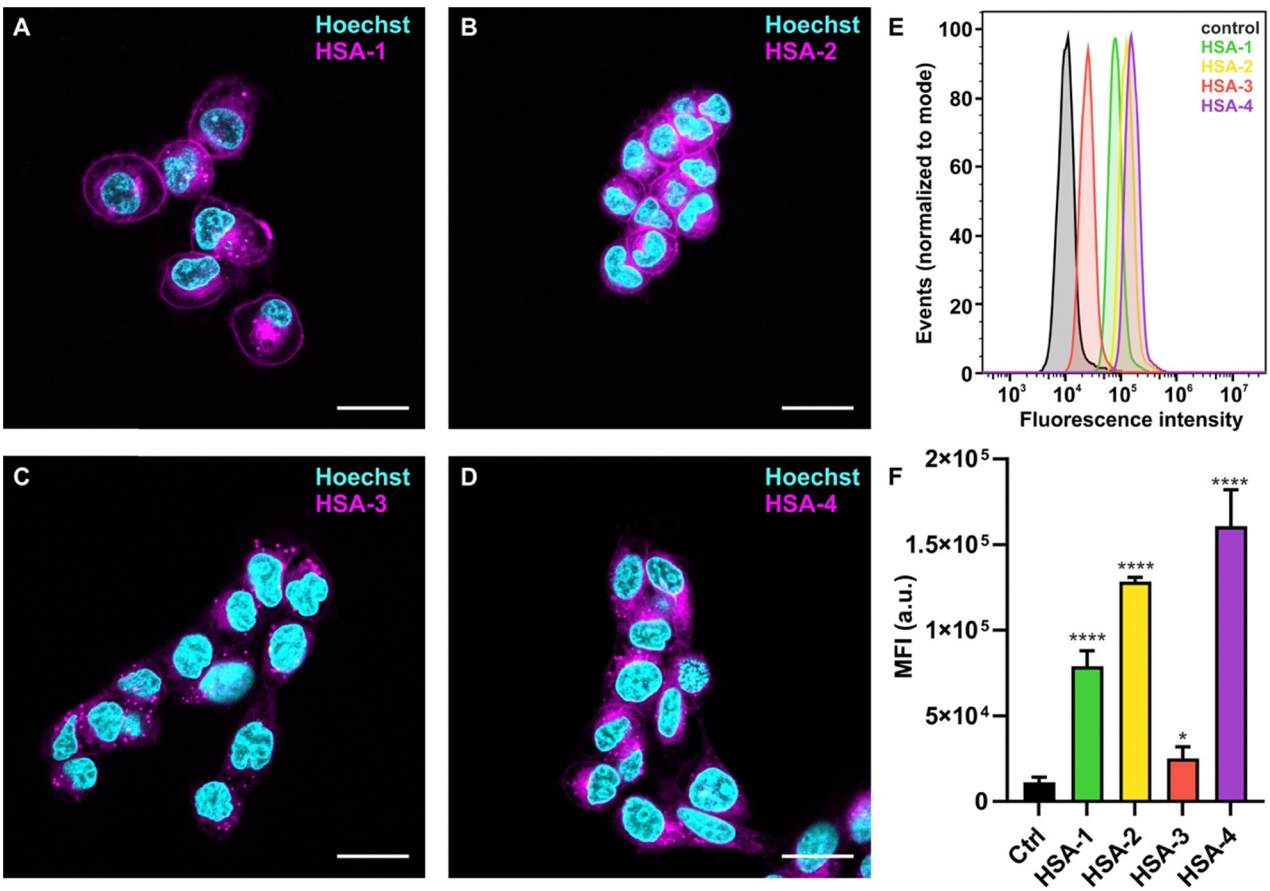

Fig. 6 Targeting the HSA–OT bioconjugates on the A431 cell line. Confocal microscopy images of cells after incubation for 45 min with HSA–OT bioconjugates at equivalent concentration of the OT molecules (1 μM). (A)–(D) Merged images of nuclei, colored in cyan, and OT fluorescence in magenta. Scale bar = 20 μm. Flow cytometry results expressed as (E) the histogram of fluorescence peaks. (F) Mean fluorescence intensity (MFI). Statistical significance was calculated by one-way parametric ANOVA followed by Dunnet's multiple comparison, * $p < 0.05$; **** $p < 0.0001$.

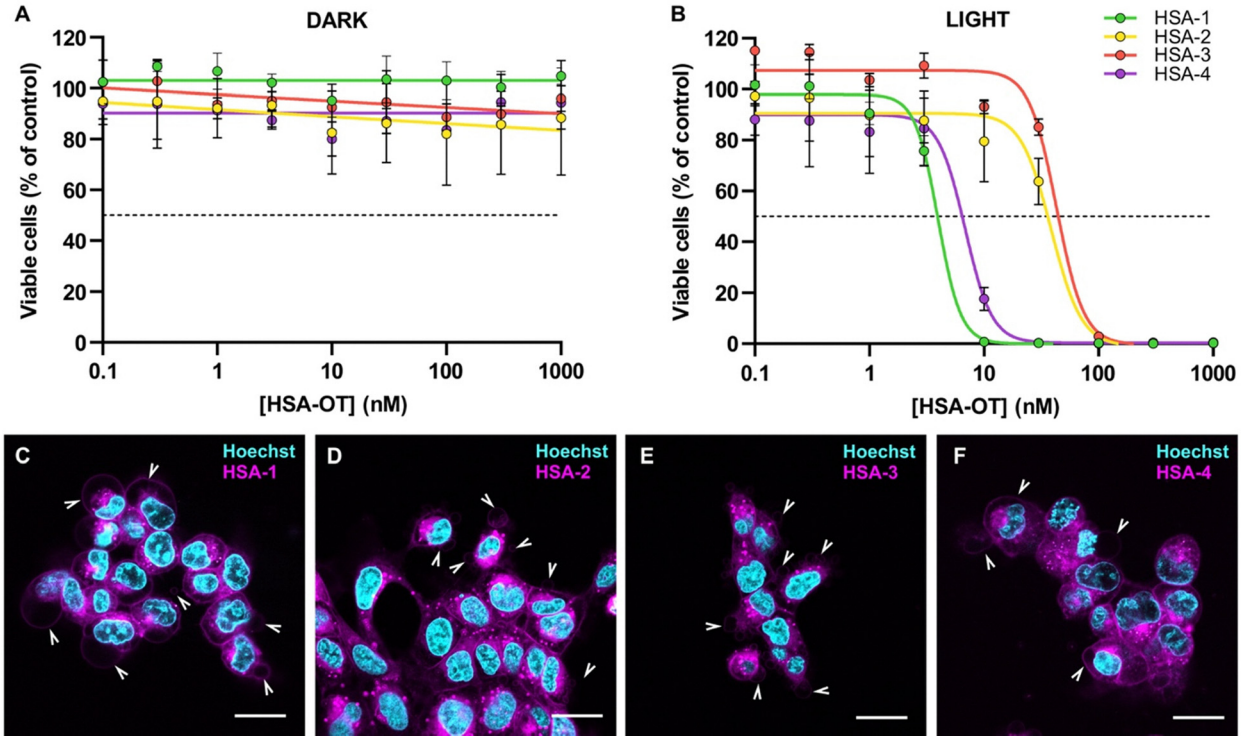

Fig. 7 Photo-dependent cytotoxicity on cancer cells treated with HSA–OT bioconjugates. A431 cells incubated for 45 min with HSA–OT bioconjugates were (A) kept under dark conditions or (B) irradiated for 10 min with white LED light, and cell viability was evaluated 24 h after the treatment. Data are shown as mean ± SD of 3 independent experiments and results are expressed as the percentage of control (untreated – dark). Real-time monitoring of the photodamage induced by (C) HSA-**1**, (D) HSA-**2**, (E) HSA-**3**, and (F) HSA-**4** on A431 cells over time. Images were acquired 10 minutes after irradiation. Panels (C)–(F) are merged images, nuclei are stained with Hoechst and colored in cyan while HSA–OT fluorescence is in magenta. The white arrows highlight the membrane blebbing process. Scale bar = 20 μm.

(IC_{50} = 42.9 nM). Compounds **1**, **2**, and **4** generate similar total ROS; yet, compound **2** exhibits lower photoactivity, as this depends on many factors, such as the albumin conjugation stoichiometry, the cellular uptake of the bioconjugate, and/or its intracellular localization during ROS production.

Time lapse imaging of the A431 cells, incubated with HSA–OT and exposed to white light, revealed for all the compounds a membrane blebbing on the cells during the irradiation process (Fig. 7C–F). Membrane blebbing is a structural modification caused by oxidative stress that spares intracellular organelles, leading to a unique necrotic-like cell death that is highly immunogenic (photoimmunotherapy). In fact, the blebbing phenomenon facilitates the release of damage-associated molecular patterns (DAMPs), such as ATP, enhancing immune activation.[33] Indeed, we recorded a 2.5-fold increase in extracellular ATP after 6 h and 2.1-fold increase after 24 h from treatment with HSA-**1** at the IC_{50} concentration (Fig. 8), representing a significant "find me" signal for dendritic cells.

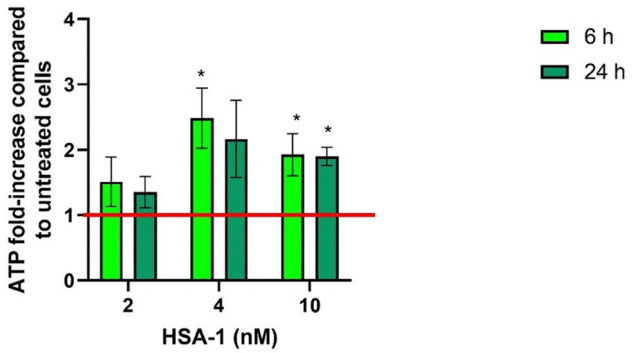

Fig. 8 ATP extracellular release 6 and 24 h after treatment of A431 cells incubated for 45 min with the HSA-**1** bioconjugate irradiated for 10 min with white LED light. Data are shown as mean ± SEM of 4 independent experiments and results are expressed as fold-increase compared to untreated cells (red line). Statistical analysis was performed using the *t*-test. * $p < 0.05$ compared to untreated cells.

This rapid and selective tumor cell destruction makes HSA–OT bioconjugates promising agents for targeted cancer photoimmunotherapy.[34,35] Thanks to the intrinsic fluorescence of the OT molecules all the investigations are label-free, and the HSA–OT bioconjugates function as a real-time self-reporting platform. The observed results warrant further validation *in vivo*, with particular emphasis on assessing immunogenicity and therapeutic efficacy under physiologically relevant conditions.

Conclusions

In summary, our work demonstrates the successful design, synthesis, and evaluation of a new class of push–pull

oligothiophene photosensitizers tailored for photodynamic therapy (PDT). Exploring positional isomers opens new avenues for discovering materials and drugs with optimized or novel functionalities, underscoring its importance as a strategic tool in molecular design and synthesis.

Through systematic modulation of the donor–acceptor architecture, particularly by shifting the position of the benzothiadiazole (Bz) acceptor unit within the oligothiophene backbone, we achieved tunable electronic, optical, and photochemical properties, as evidenced by the progressive red shift in both absorption and emission spectra and the corresponding reduction of the HOMO–LUMO energy gap.

Computational studies suggested that all the OT derivatives (compounds **1–4**) are capable of generating reactive oxygen species *via* both type I and type II mechanisms. In particular, high spin–orbit coupling constant values were calculated for all the compounds.

These predictions were validated by experimental assays. An amine reactive *N*-hydroxysuccinimide ester was installed on the designed oligothiophenes, for conjugation to human serum albumin (HSA–OT).

HSA–OT bioconjugates were water-soluble, highly photoactive, and biocompatible. These bioconjugates preserved the intrinsic fluorescence of the OTs, enabling real-time imaging and tracking in biological systems. Cellular uptake studies in A431 carcinoma cells revealed effective internalization of all conjugates. Upon light activation, all HSA–OT conjugates triggered robust ROS production, resulting in potent phototoxic effects and complete cancer cell eradication with minimal dark toxicity. Particularly HSA-**1** and HSA-**4**, characterized respectively by an A–D and D–A architecture, were active at very low concentration of the photosensitizer (IC_{50} = 4.0 nM for HSA-**1** and IC_{50} = 7.3 nM for HSA-**4**), outperforming the benchmark HSA-**2** compound (IC_{50} = 38.6 nM) and HSA-**3** (IC_{50} = 42.9 nM) characterized by a D–A–D architecture.

The observed membrane blebbing during irradiation suggests a necrotic-like cell death accompanied by potential immunogenic effects, paving the way for the use of HSA–OT bioconjugates in photoimmunotherapy.

Collectively, these findings underscore the versatility of push–pull oligothiophene architectures in creating effective theranostic agents for targeted cancer treatment. Future investigations will focus on *in vivo* evaluation and immune system activation to fully exploit the therapeutic potential of the HSA–OT bioconjugates.

Author contributions

Conceptualization: M. C., F. D. M; data curation: M. D. G; formal analysis: M. C., F. D. M., M. D. G; funding acquisition: M. C.; investigation: S. F., M. D. S., P. E. C., E. J. M., A. M., E. T., S. L. R., M. M., T. D. M., M. N., N. S., A. Z., M. Z; methodology: M. C., F. D. M., M. D. G; resources: A. D., M. C., F. D. M.; supervision: A. D., M. C., F. D. M.; writing – review and editing: S. F., M. D. S., P. E. C., E. J. M., M. Z., A. D., M. D. G., F. D. M., M. C.

Conflicts of interest

There are no conflicts to declare.

Data availability

The data supporting this article have been included as part of the SI. (i) Synthesis of the compounds **1**,**3**,**4**; (ii) NMR spectra; (iii) absorption and emission maxima, Stokes shift, molar extinction coefficients (ε) and fluorescence quantum yields (φ_{em}) of compounds **1–4**; (iv) computational details; (v) UV-Vis absorption spectra of the compounds **1–4** in DMF (simulated and acquired experimentally by UV-Vis); (vi) ESP charges; (vii) calculated natural transition orbitals (NTO); (viii) optimized geometries of the ground state S_0, the first excited singlet state S_1 and the first excited triplet state T_1; (ix) dihedral angles φ (degree) of compounds **1–4** in the S_0, S_1 and T_1 minima, calculated in DMF; (x) redox potentials and reduction peak voltage (in V *vs.* SCE at 0.1 V s^{-1}) of compounds **1–4**; (xi) synthesis and characterization of HSA–OT bioconjugates; (xii) UV-Vis absorption spectra of the compounds **1–4** in DMF and their corresponding HSA–OT bioconjugates in PBS; (xiii) UV-Vis absorption and emission spectra of compounds HSA-**1**, HSA-**2**, HSA-**3** and HSA-**4** in PBS; (xiv) relative quantum yields (φ_{em}) in PBS solutions calculated using $[Ru(bpy)_3]Cl_2$ as reference. See DOI: **https://doi.org/10.1039/d5tb01076d**.

Acknowledgements

The research leading to these results has received funding from AIRC under MFAG 2019 – ID. 22894 project (M. C.) E. J. M and T. D. M. were supported by Fondazione Umberto Veronesi. M. Z. and F. D. M. acknowledge the project LiveAir Force Office of Scientific Research (AFOSR) Projects FA8655-22-1-7014, and the PRIN project EMBRACE (IntErLocked supraMolecular assemBlies in solution: the access key to new donoR–Acceptor multiComponent architEctures, CUP number: B53D23015460006).

References

1 B. Lu, Y. Huang, Z. Zhang, H. Quan and Y. Yao, *Mater. Chem. Front.*, 2022, **6**, 2968–2993, DOI: **10.1039/d2qm00752e**.
2 L. Wang and W. Zhu, *Adv. Sci.*, 2024, **11**, 2307227, DOI: **10.1002/advs.202307227**.
3 J. Deckers, T. Cardeynaels, S. Doria, N. Tumanov, A. Lapini, A. Ethirajan, M. Ameloot, J. Wouters, M. Di Donato, B. Champagne and W. Maes, *J. Mater. Chem. C*, 2022, **10**, 9344–9355, DOI: **10.1039/d2tc01526a**.
4 L. Li, G. Yuan, Q. Qi, C. Lv, J. Liang, H. Li, L. Cao, X. Zhang, S. Wang, Y. Cheng and H. He, *J. Mater. Chem. B*, 2022, **10**, 3550–3559, DOI: **10.1039/d1tb02598h**.
5 S. M. Sartor, B. G. McCarthy, R. M. Pearson, G. M. Miyake and N. H. Damrauer, *J. Am. Chem. Soc.*, 2018, **140**, 4778–4781, DOI: **10.1021/jacs.8b01001**.

6 R. Singh, D. G. Chen, C. H. Wang, C. C. Wu, C. H. Hsu, C. H. Wu, T. Y. Lai, P. T. Chou and C. T. Chen, *J. Mater. Chem. B*, 2022, **10**, 6228–6236, DOI: 10.1039/d2tb01224c.
7 M. De Li, Z. Yan, R. Zhu, D. L. Phillips, I. Aparici-Espert, V. Lhiaubet-Vallet and M. A. Miranda, *Chem. – Eur. J.*, 2018, **24**, 6654–6659, DOI: 10.1002/chem.201800716.
8 P. Liu, X. Zhao, J. Cao, M. Tian, Y. Li, C. Ma, T. Yang and Y. Liu, *J. Mater. Chem. B*, 2024, **12**, 7870–7878, DOI: 10.1039/d4tb00814f.
9 R. Wang, X. Li and J. Yoon, *ACS Appl. Mater. Interfaces*, 2021, **13**, 19543–19571, DOI: 10.1021/acsami.1c02019.
10 S. Fuse, M. Takizawa, K. Matsumura, S. Sato, S. Okazaki and H. Nakamura, *Eur. J. Org. Chem.*, 2017, 5170–5177, DOI: 10.1002/ejoc.201701019.
11 A. Cantelli, M. Malferrari, A. Soldà, G. Simonetti, S. Forni, E. Toscanella, E. J. Mattioli, F. Zerbetto, A. Zanelli, M. Di Giosia, M. Zangoli, G. Barbarella, S. Rapino, F. Di Maria and M. Calvaresi, *JACS Au*, 2021, **1**, 925–935, DOI: 10.1021/jacsau.1c00061.
12 P. E. Costantini, R. Saporetti, M. Iencharelli, S. Flammini, M. Montrone, G. Sanità, V. De Felice, E. J. Mattioli, M. Zangoli, L. Ulfo, M. Nigro, T. Rossi, M. Di Giosia, E. Esposito, F. Di Maria, A. Tino, C. Tortiglione, A. Danielli and M. Calvaresi, *Small*, 2025, **21**, 2405832, DOI: 10.1002/smll.202405832.
13 N. Cao, Y. Jiang, Z. B. Song, D. Chen, D. Wu, Z. L. Chen and Y. J. Yan, *Eur. J. Med. Chem.*, 2024, **264**, 116012, DOI: 10.1016/j.ejmech.2023.116012.
14 J. J. Alcázar, *Int. J. Mol. Sci.*, 2024, **25**, 2528, DOI: 10.3390/ijms25052528.
15 B. A. D. Neto, J. R. Correa and J. Spencer, *Chem. – Eur. J.*, 2022, **28**, e202103262, DOI: 10.1002/chem.202103262.
16 R. F. Veríssimo, P. H. F. Matias, M. R. Barbosa, F. O. S. Neto, B. A. D. Neto and H. C. B. de Oliveira, *J. Chem. Inf. Model.*, 2025, **65**, 7874–7886, DOI: 10.1021/acs.jcim.4c02414.
17 M. S. Baptista, J. Cadet, P. Di Mascio, A. A. Ghogare, A. Greer, M. R. Hamblin, C. Lorente, S. C. Nunez, M. S. Ribeiro, A. H. Thomas, M. Vignoni and T. M. Yoshimura, *Photochem. Photobiol.*, 2017, **93**, 912–919, DOI: 10.1111/php.12716.
18 M. Hayyan, M. A. Hashim and I. M. Alnashef, *Chem. Rev.*, 2016, **116**, 3029–3085, DOI: 10.1021/acs.chemrev.5b00407.
19 W. H. Yin, Y. Liu, H. H. Huang, P. Y. Li, X. Liu and F. Q. Bai, *J. Org. Chem.*, 2025, **90**, 1825–1834, DOI: 10.1021/acs.joc.4c02428.
20 X. Wang, F. Q. Bai, Y. Liu, Y. Wang, H. X. Zhang and Z. Lin, *J. Chem. Inf. Model.*, 2017, **57**, 1089–1100, DOI: 10.1021/acs.jcim.7b00142.
21 G. Barbarella, M. Zangoli and F. Di Maria, *Adv. Heterocycl. Chem.*, 2017, **123**, 105–167, DOI: 10.1016/bs.aihch.2017.01.001.
22 M. Marinelli, A. Candini, F. Monti, A. Boschi, M. Zangoli, E. Salatelli, F. Pierini, M. Lanzi, A. Zanelli, M. Gazzano and F. Di Maria, *J. Mater. Chem. C*, 2021, **9**, 11216–11228, DOI: 10.1039/d1tc02641k.
23 I. Palamà, F. Di Maria, I. Viola, E. Fabiano, G. Gigli, C. Bettini and G. Barbarella, *J. Am. Chem. Soc.*, 2011, **133**, 17777–17785, DOI: 10.1021/ja2065522.
24 M. Zangoli, M. Gazzano, F. Monti, L. Maini, D. Gentili, A. Liscio, A. Zanelli, E. Salatelli, G. Gigli, M. Baroncini and F. Di Maria, *ACS Appl. Mater. Interfaces*, 2019, **11**, 16864–16871, DOI: 10.1021/acsami.9b02404.
25 M. Zambianchi, A. Barbieri, A. Ventola, L. Favaretto, C. Bettini, M. Galeotti and G. Barbarella, *Bioconjug. Chem.*, 2007, **18**, 1004–1009, DOI: 10.1021/bc060332e.
26 Z. Zhuang, J. Li, P. Shen, Z. Zhao and B. Z. Tang, *Aggregate*, 2024, **5**, e540, DOI: 10.1002/agt2.540.
27 L. Ulfo, A. Cantelli, A. Petrosino, P. E. Costantini, M. Nigro, F. Starinieri, E. Turrini, S. K. Zadran, G. Zuccheri, R. Saporetti, A. Danielli and M. Calvaresi, *Nanoscale*, 2022, **14**, 632–641, DOI: 10.1039/D1NR06053H.
28 A. Petrosino, R. Saporetti, F. Starinieri, E. Sarti, L. Ulfo, L. Boselli, A. Cantelli, A. Morini, S. K. Zadran, G. Zuccheri, Z. Pasquini, M. Di Giosia, L. Prodi, P. P. Pompa, P. E. Costantini, M. Calvaresi and A. Danielli, *iScience*, 2023, **26**, 108032, DOI: 10.1016/j.isci.2023.108032.
29 B. Bortot, M. Apollonio, G. Baj, L. Andolfi, L. Zupin, S. Crovella, M. di Giosia, A. Cantelli, R. Saporetti, L. Ulfo, A. Petrosino, G. Di Lorenzo, F. Romano, G. Ricci, M. Mongiat, A. Danielli, M. Calvaresi and S. Biffi, *Free Radic. Biol. Med.*, 2022, **179**, 242–251, DOI: 10.1016/j.freeradbiomed.2021.11.019.
30 E. Turrini, L. Ulfo, P. E. Costantini, R. Saporetti, M. Di Giosia, M. Nigro, A. Petrosino, L. Pappagallo, A. Kaltenbrunner, A. Cantelli, V. Pellicioni, E. Catanzaro, C. Fimognari, M. Calvaresi and A. Danielli, *Cell. Mol. Life Sci.*, 2024, **81**, 144, DOI: 10.1007/s00018-024-05174-7.
31 A. Trifoglio, F. Tunioli, L. Favaretto, M. Zambianchi, C. Bettini, I. Manet, L. Mariani, A. Barra Caracciolo, P. Grenni, M. Di Sante, M. Di Giosia, T. D. Marforio, E. J. Mattioli, M. Calvaresi and M. Melucci, *J. Mater. Chem. A*, 2025, **13**, 4587–4599, DOI: 10.1039/d4ta06689h.
32 G. Greco, L. Ulfo, E. Turrini, A. Marconi, P. E. Costantini, T. D. Marforio, E. J. Mattioli, M. Di Giosia, A. Danielli, C. Fimognari and M. Calvaresi, *Cells*, 2023, **12**, 392, DOI: 10.3390/cells12030392.
33 L. Galluzzi, I. Vitale, S. Warren, S. Adjemian, P. Agostinis, A. B. Martinez, T. A. Chan, G. Coukos, S. Demaria and E. Deutsch, *et al.*, *J. Immunotherap. Cancer.*, 2020, **8**, e000337, DOI: 10.1136/jitc-2019-000337.
34 H. Kobayashi and P. L. Choyke, *Acc. Chem. Res.*, 2019, **52**, 2332–2339, DOI: 10.1021/acs.accounts.9b00273.
35 Y. Zhang, X. Chen, C. Gueydan and J. Han, *Cell Res.*, 2018, **28**, 9–21, DOI: 10.1038/cr.2017.133.